

Asymmetry, bistability, and vortex dynamics in a finite-geometry ferromagnet-superconductor bilayer structure

G. Carapella,* P. Sabatino, and G. Costabile

CNR-INFM "SUPERMAT," Dipartimento di Matematica e Informatica, Università di Salerno,
via Ponte don Melillo, I-84084 Fisciano, Italy

(Received 30 October 2009; revised manuscript received 29 December 2009; published 5 February 2010)

We have recently demonstrated that Py/Nb bilayers patterned in a strip geometry can exhibit asymmetric transport properties and bistability. Here, with the help of numerical simulations in the framework of time-dependent Ginzburg-Landau model for superconductor and Landau-Lifshitz-Gilbert model for ferromagnet, it is demonstrated that the asymmetric and bistable magnetotransport response of the bilayers can be accounted for by the stray fields from the patterned ferromagnetic layer. Numerical simulations on vortex dynamics show that in the dissipative branch of the bilayer a peculiar spontaneous channeled flux flow regime is realized, with alternating vortex and antivortex chains moving in the opposite directions in the superconducting layer.

DOI: [10.1103/PhysRevB.81.054503](https://doi.org/10.1103/PhysRevB.81.054503)

PACS number(s): 74.78.Fk, 74.20.De, 75.70.Kw, 74.25.Ha

I. INTRODUCTION

In the past years the ferromagnet/superconductor (FS) hybrids¹⁻³ based both on oxide and metallic thin film have attracted a lot of interest, also due to the possibility to control superconductivity by the exchange field,^{1,4,5} spin imbalance,⁶⁻⁹ or by the stray fields generated by the ferromagnet.¹⁰⁻¹⁶ Recently, FS heterostructures have also been proposed¹⁷⁻²⁰ for the realization of superconducting rectifiers²¹⁻²⁹ less technologically demanding and with enhanced power handling capability. Ferromagnetic materials where stripe domain magnetic structure is achieved have been demonstrated to be very effective to control superconductivity³⁰⁻³² at submicron scale. Very recently Permalloy-based FS hybrids with Permalloy in the weak stripe domain regime³³ have been demonstrated to induce *anisotropic* transport properties^{34,35} and to act as guiding channels³⁶ for Abrikosov vortices in the superconducting layer.

Recently, we have demonstrated²⁹ that a Py/Nb bilayer, patterned in a Hall geometry and with Py in the stripe domain regime, can exhibit strongly asymmetric and bistable transport properties, i.e., it can behave as a bistable superconducting diode. Here we discuss some additional relevant experimental data and, with the help of numerical simulations, we discuss in detail and more quantitatively the main physical mechanism involved in the bistable diode. Numerical simulations substantially confirm the hypothesis²⁹ that the observed bistable diode behavior can be accounted for by the stray fields from the patterned ferromagnetic layer. Moreover, using the two-dimensional time-dependent Ginzburg-Landau equation, in the present work we also numerically address in detail the vortex dynamics involved in a superconducting film embedded in the inhomogeneous magnetic field generated by a finite-geometry ferromagnetic bar in the stripe domain regime. The main result of vortex dynamic simulations is that, at zero externally applied magnetic field and with current applied perpendicular to the magnetic stripes, a peculiar channeled flux flow regime is achieved, with alternating vortex and antivortex chains moving in the opposite directions in the superconducting layer. Such a re-

gime reminds the one reported in recent works^{37,38} done in other FS heterostructures, where a periodic array of micrometer size ferromagnetic bars was used to create two channels of opposite polarity for vortex-antivortex chains. In our case, these channels are naturally created by the stray fields of the continuous Py film in the stripe domain regime. When current is applied along the magnetic stripes, another dissipative mechanism is realized, consisting of creation of vortex-antivortex pairs in the channels followed by a Lorentz force-assisted vortex-antivortex pairs annihilation.

The work is organized as follow. In Sec. II, after a very brief summary of the main experimental results,²⁹ we present and discuss some supplementary results useful to gain insight in the physics involved in the system. In Sec. III, we first analyze numerically the distribution of stray fields from the finite-geometry ferromagnetic layer and then study the transport properties of the thin superconducting layer embedded in the inhomogeneous magnetic field generated by the ferromagnetic layer. Micromagnetic simulation are performed assuming the Landau-Lifshitz-Gilbert model for ferromagnet and the transport properties of the superconductor are simulated using the two-dimensional time-dependent Ginzburg-Landau equation. A summary of the main results is given in Sec. IV.

II. BASIC PHENOMENOLOGY AND DISCUSSION

The focus of this work is on numerical study of working mechanisms of the bistable vortex diode. Here we only recall two relevant experimental facts already published in our recent work and we add some experiments that help us to discuss the physics involved in the diode. For further experimental results and details we refer the reader at Ref. 29.

In Fig. 1(a) we show the $V(I)$ curve of a Py(640 nm)/Nb(60 nm) bilayer²⁹ in the full voltage range, recorded at 4.6 K (superconducting state) and at 6.0 K (normal state). The critical currents (I_{CP} and I_{CN} , the current values at which the transition to the fully normal state is achieved) are found to differ slightly, around 20%. In the bottom frame of Fig. 1(a) we show a blow up of the low-voltage region of the $V(I)$ curve at 4.6 K. Two rather different depinning currents (I_{DP} ,

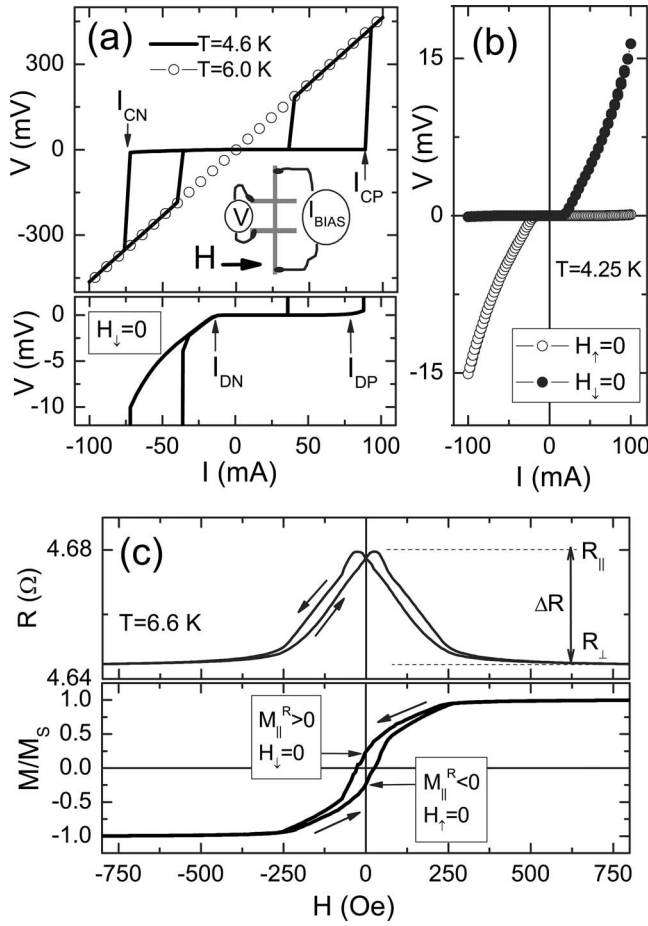


FIG. 1. (a) The $V(I)$ curve of the Py/Nb bilayer in the full voltage range at 4.6 K (superconducting state) and at 6.0 K (normal state). The geometry of the bilayer is shown in the insets. The $V(I)$ curve at 4.6 K with amplified low-voltage range exhibits two quite different depinning currents, as shown in the bottom panel. (b) $V(I)$ curve of the device recorded in the two possible stable states at $H = 0$. (c) The AMR of the device at temperature slightly larger than the critical temperature of the Nb. The normalized hysteresis loop of the bilayer calculated from the above AMR signal is shown in the bottom panel.

and I_{DN} , the current values corresponding to the transition $V=0 \rightarrow V \neq 0$ are exhibited. Due to two substantially different depinning currents, the bilayer exhibits infinite or finite conductance depending on the sign of the bias current so that it behaves like a superconducting diode (the dual of a semi-conducting diode). The $V(I)$ curve in Fig. 1(a) was recorded after a preparing magnetic field was applied in the plane of the device, as shown in the inset, and was decreased from a relatively large positive value ($H = 1000$ Oe) toward $H = 0$, at which value the curve was recorded. Here and in the following we shall use $H_{\uparrow} = 0$ to mean that the in-plane magnetic field was started from large negative values and $H_{\downarrow} = 0$ to mean that the field was started from large positive values. The $V(I)$ curves of the device recorded at $H_{\uparrow} = 0$ and $H_{\downarrow} = 0$ are plotted²⁹ in Fig. 1(b). We emphasize that the $V(I)$ curve in the magnetic state at $H_{\uparrow} = 0$ is mirrored with respect to the origin in the other stable magnetic state at $H_{\downarrow} = 0$, i.e., the $V(I)$ of the FS bilayer is not only asymmetric but also

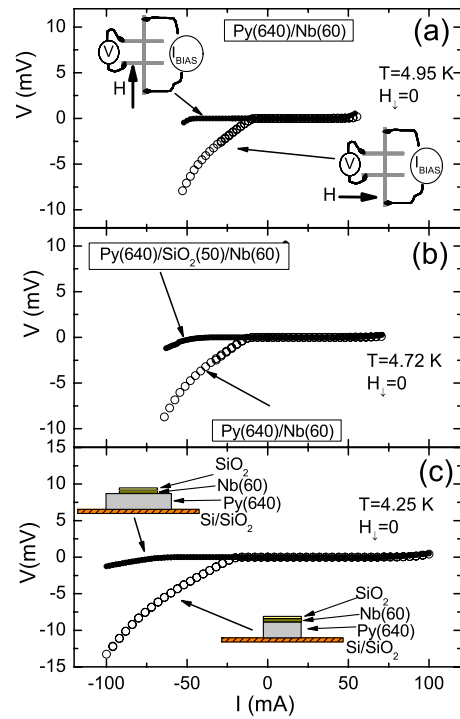


FIG. 2. (Color online) (a) Comparison of $V(I)$ curves of the Py(640)/Nb(60) bilayer recorded at 4.95 K with preparing magnetic field applied along or perpendicular to the bias current, as shown in the insets. (b) $V(I)$ curves of a Py(640)/Nb(60) and a Py(640)/SiO₂(50)/Nb(60) bilayer at 4.72 K. Bias current is perpendicular to the preparing field. (c) $V(I)$ curves at 4.25 K for two Py(640)/Nb(60) bilayers having the Py of same width as (see lower inset) or larger width than (see top inset) the Nb layer.

bistable. With respect to the full hysteresis loop of the Py, these two states correspond to the two possible in-plane remanent magnetizations, $M_{\parallel}^R > 0$ at $H_{\downarrow} = 0$, and $M_{\parallel}^R < 0$ at $H_{\uparrow} = 0$, as it is better seen in Fig. 1(c), where we show the normalized hysteresis loop of the Py at 6.6 K (bottom panel) calculated³⁹ from the anisotropic magnetoresistance (AMR) signal (top panel) of the bilayer. The hysteresis loop $M(H)$ was extracted from the $R(H)$ measured for magnetic field applied perpendicular to the current by means of relation $M/M_S = \pm \sqrt{[R_{\parallel} - R(H)]/\Delta R}$, where the symbols are the ones shown in Fig. 1(c). This relation is obtained from AMR relation³⁹ $R(\theta) = R_{\perp} + \Delta R \cos^2(\theta)$, where θ is the angle between magnetization and current density that, for polycrystalline materials as it is our sputtered Py, can also be recast in the form $R(H) = R_{\parallel} - \Delta R (M/M_S)^2$, with M the component of magnetization along the magnetic field direction.

In Fig. 2 we report some other experimental results that can be useful to gain insight into the origin of the observed asymmetric and bistable behavior of the bilayer. In Fig. 2(a) we compare the $V(I)$ curves of the Py(640 nm)/Nb(60 nm) bilayer recorded at 4.95 K with the preparing magnetic field applied either along or perpendicular to the bias current. Apparently, the asymmetry of depinning currents does not occur when the preparing field is parallel to the bias current. For magnetic field perpendicular to the bias current, the asymmetry was found to be strongly reduced if the Py and Nb layers

were spaced by a 50-nm-thick SiO₂, as shown in Fig. 2(b). A substantial reduction in asymmetry was also observed when in the bilayer the width of the bottom Py layer was made larger than the width of the top Nb layer. This is seen in Fig. 2(c), where we compare the $V(I)$ curves of a bilayer with same width for Py and Nb (both 100 μm wide) versus a bilayer with 200- μm -wide Py and 100- μm -wide Nb.

As discussed in Ref. 29, we observed asymmetry in samples with 480- or 640-nm-thick Py but not in a sample with 180-nm-thick Py. This suggests that in the thicker samples the Py might be in the stripe domains regime.^{33,36} From magnetic measurements performed with a vibrating-sample magnetometer we estimated²⁹ a perpendicular anisotropy constant $K_u=9 \times 10^4$ erg/cm³ and a critical thickness for stripe domains^{33,36} $t_c \approx 210$ nm for our Py at $T=10$ K. This agrees with the hypothesis that a stripe domain structure builds up in the thicker samples but not in the 180-nm-thick Py sample. The stripe width can be estimated³⁶ from above data as $d \approx 240$ nm. The critical thickness of our Py is similar to the one reported^{33,36} in recent works, where it has been demonstrated that a well-developed stripe domain regime is in fact achieved beyond the above estimated critical thickness.

Magnetic data suggest that the mechanism accounting for the bistable diode behavior could involve the stray fields from the patterned Py layer in the stripe domain. Before we proceed further, we shall comment other two known mechanisms that also generate asymmetric $V(I)$ curves. The simple mechanism¹⁹ based on fringe fields at edges of the FS bilayers that add to the self-fields of transport current cannot account for all of our experimental results. If such a mechanism were the most relevant, the asymmetry should increase with magnetic field,¹⁷ as the fringe fields are stronger in the fully in-plane magnetically saturated state. Inspection of Fig. 1(d) of our previous work²⁹ suggests that this is not our case. Moreover, an asymmetry should be observed also for the 180-nm-thick Py sample. This, again, is not our case. We also think that our results are not accounted for by the mechanism of asymmetric surface barrier.^{21,22} Though here we have asymmetric boundary conditions for Nb, we should admit that the in-plane magnetic field generates vortices with flux lines in the plane of the Nb film so that Lorentz force pushes them out of the film, along its thickness, to experience the surface barriers. This is very unlikely in our case because the Nb film is thinner than the London penetration length, as opposite to the experiments^{21,22} where Pb/Pb_{0.95}Tl_{0.5} ribbons much thicker than London penetration length in those materials were used. However, if present, this mechanism should be effective^{21,22} only for in-plane magnetic field $H_{c1}^{\parallel} < H < H_{c2}^{\parallel}$. In our Nb film these critical fields are estimated to be equal to several thousand Oe. Instead, we observe strong asymmetry also without any externally applied magnetic field. Moreover, we should observe asymmetry even if the Py layer were made thinner than the critical thickness for nucleation of a stripe domain regime or if its width were larger than the width of the Nb strip. As said above, this was not our case.

In our Py layers the strength of stray fields from weak stripe domain is estimated⁴⁰ to be lower than the critical field $H_{c1} \approx 300$ Oe of our Nb at 4.2 K. Thus, these stray fields can

act only as a periodic potential that can channel the Abrikosov vortices or antivortices however generated in the Nb. The channeling effect³⁶ of the stripes in the Py can be expected because the estimated stripe width is larger than the size of the vortices, i.e., $d \geq 2\lambda_L$, as London penetration depth of our Nb was estimated to be $\lambda_L \approx 100$ nm at 4.25 K. In the above reported experimental data, the direction of channels was set³⁶ by the preparing field applied perpendicular to the transport current. But, what generates Abrikosov vortices, with flux lines perpendicular to the Nb film, that the Lorentz force associated to a transport current can move along the plane of the film in the channels so generating a voltage? A source of such vortices can be the perpendicular component of stray fields at edges of the patterned ferromagnetic strip that adds to the stray fields from stripe domains.

III. NUMERICAL SIMULATIONS

To make more clear the above picture, we numerically studied the distribution of stray fields from a patterned ferromagnetic layer and the response of a thin superconducting layer to the inhomogeneous magnetic field generated by the ferromagnetic layer.

A. Micromagnetics

Micromagnetic simulations were performed using the three-dimensional OOMMF micromagnetic simulation package,⁴¹ based on Landau-Lifshitz-Gilbert equation for ferromagnets. A Py slab of width $W=1960$ nm, length $L=1460$ nm, and thickness $d=480$ nm was chosen. Lateral physical dimensions were chosen to retain relevant information within capabilities of our computer (an Intel I7 940 quad core processor with 4 GB RAM). The cell size was $\Delta x=20$ nm, $\Delta y=10$ nm, and $\Delta z=10$ nm. The perpendicular anisotropy was $K_u=3 \times 10^5$ erg/cm³, slightly larger than, though comparable to, the experimental one. The magnetic field was applied in the plane of the slab, along the x direction, and the states $H_{x\downarrow}=0$ and $H_{x\uparrow}=0$ were studied, with emphasis on the distribution of the out-of-plane (i.e., along the z direction) component of the stray fields.

In Fig. 3(a) we show the calculated distribution of the perpendicular component of the magnetization in the remanent state (achieved at $H_{x\downarrow}=0$) of the Py slab with anisotropy along z axis. The stripe domain regime with alternating up (brighter regions) and down (darker regions) magnetization occurs with the used parameters. In Fig. 3(b) we show the vectorial distribution of the total magnetic field in a cross section in the z - y plane centered in the middle (i.e., at $x=W/2$) of the Py slab. Stray fields on the top of the slab appear to be periodic along the length (y direction) of the slab with a spatial period 2ℓ , where $\ell \approx 250$ nm is the stripe width.

Further details about the stray fields on the top of the slab, that are the fields affecting the Nb layer, are given in Fig. 4. In Fig. 4(a) we report the calculated in-plane hysteresis loop of the Py slab and the spatial distribution of the out-of-plane component (z component) of stray fields on the top face of the slab for the two remanent states. In the bright (dark)

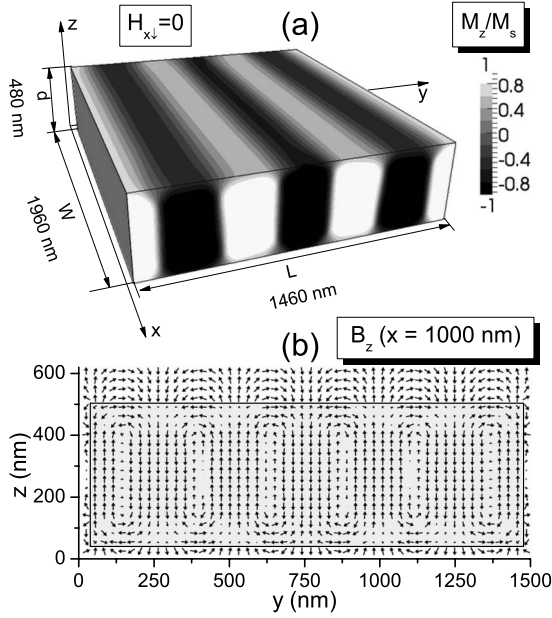


FIG. 3. (a) Calculated distribution of the perpendicular component of the magnetization in the remanent state (achieved at $H_{x\downarrow} = 0$) of a Py slab with anisotropy along z axis showing stripes domains. (b) Calculated vectorial distribution of total magnetic field in a slice in the z - y plane centered in the middle of the Py slab. Both the field in Py (shaded region) and the field out of Py (stray field) are shown.

regions the field points to the positive (negative) z direction. At the edges of the slab the intensity of the stray field is larger than at the center, with role of edges inverted in the two remanent states. In Fig. 4(b) we plot the out-of-plane component of the stray field 40 nm above the slab, scanned along the three different lines labeled as α , β , and γ in the upper inset in Fig. 4(a). The intensity of stray fields is about 270 G at the center of the slab but peaks to about 600 G at the right edge and -600 G at the left edge. In other words, to the stray field at the center of the slab, a field B_{0z} is added near the right edge and a field $-B_{0z}$ is added near the left edge. This modulation of stray fields along the x direction (i.e., the direction of stripes we set with applied field H_x) is accounted for by the Bloch domain walls separating the up and down stripe domains we can envisage in Fig. 3. At the domain walls a magnetization M_x along the x direction is always present and such a component generates magnetic charges (of opposite sign) at left and right edges. These magnetic charges, in a way similar to a ferromagnet without perpendicular anisotropy, produce an additional stray field with a maximum z component $\pm B_{0z}$ at edges of the slab that adds to the stray field from stripes. In a particular stripe domain, as one can see in Fig. 4(b) for a constant value of y , the total stray fields are stronger at one side while at the other side of the stripe the total stray fields are even a bit reduced. One could suspect that this kind of asymmetry in the magnetic field profile between the left and right edges of the sample breaks reflection symmetry and creates a vortex ratchet potential. But, as it will be more clear below, in our system we have not a ratchet potential,^{20,24} though the different intensity of stray fields at edges accounts for an asymmetric onset of

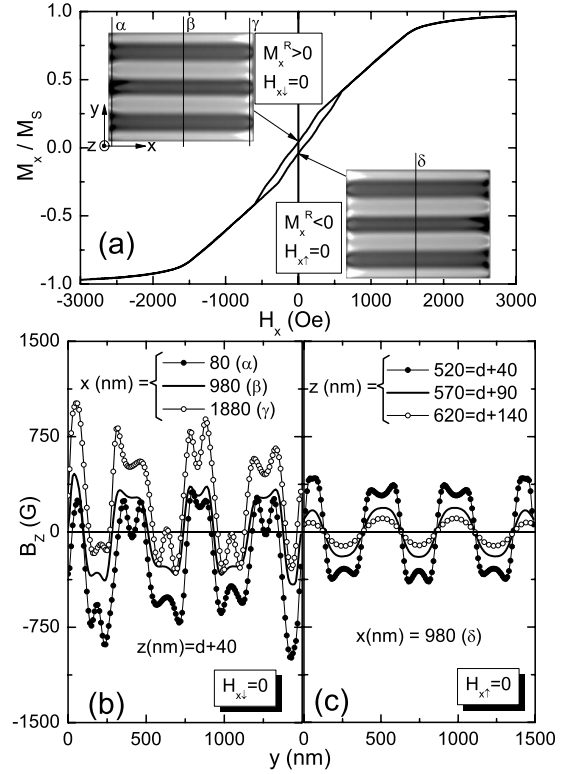


FIG. 4. (a) Calculated in-plane hysteresis loop of the Py slab. In the insets we show the distribution of out-of-plane component (z component) of stray fields (α) on the top face of the slab for the two remanent states. In the bright (dark) regions the field points in the positive (negative) z direction. At the edges of the slab, the stray field is larger than at the center with role of edges inverted in the two remanent states. (b) Out-of-plane component of stray field just above the slab scanned along the three different lines labeled as α , β , and γ in the upper inset in (a). The slab is in the remanent state achieved at $H_{x\downarrow} = 0$. (c) Out-of-plane component of stray field above the 480-nm-thick slab. The scanning is along the line labeled δ in (a) and three different z levels are shown.

vortex motion. Finally, in Fig. 4(c) we plot the stray field at center as a function of the separation from the top face of the 480-nm-thick slab. The scanning is along the line labeled δ in Fig. 4(a) and three different z levels are considered. These levels correspond to 40, 90, and 140 nm above the surface of the slab. Apparently, beside the expected amplitude reduction, the functional form of stray fields approximates a square wave near the slab and a sinusoid far from the slab in agreement with recent analytical results.⁴²

B. Vortex dynamics

To study numerically the transport properties of our thin superconducting Nb layer embedded in the stray fields of the ferromagnetic Py, we integrated the two-dimensional time-dependent Ginzburg-Landau equation supplemented with the equation for the electrostatic potential^{43,44}

$$u \left(\frac{\partial}{\partial t} + i\varphi \right) \psi = (1 - |\psi|^2) \psi - (i \nabla + \mathbf{A})^2 \psi, \quad (1)$$

$$\nabla^2 \varphi = \text{div}\{\text{Im}[\psi^*(\nabla - i\mathbf{A})\psi]\}, \quad (2)$$

where $\psi = |\psi|e^{i\phi}$ is the complex order parameter, \mathbf{A} is the vector potential, φ is the electrostatic potential, and the coefficient $u=5.79$ accounts for the relaxation of the order parameter.⁴⁵ All the physical quantities are measured in dimensionless units. The spatial coordinates are in units of the coherence length $\xi_0 = \sqrt{8k_B T_c / \pi \hbar D}$ (T_c is the critical temperature and D is the diffusion constant) and time is scaled in units of the Ginzburg-Landau relaxation time $\tau_0 = 4\pi\sigma_n \lambda_L^2 / c^2$ (σ_n is the normal-state conductivity and λ_L the magnetic field penetration depth). The order parameter is in units of $\Delta_0 = 4k_B T_c \sqrt{u}$ (the superconducting gap at $T=0$ which follows from Gor'kov's derivation of the Ginzburg-Landau equations), the vector potential is scaled in units $\Phi_0 / 2\pi\xi_0$ (Φ_0 is the quantum of magnetic flux) and the electrostatic potential is in units of $\varphi_0 = c\Phi_0 / 8\pi^2 \xi_0 \lambda_L \sigma_n$. In these units the magnetic field is scaled with $H_{c2} = \Phi_0 / 2\pi\xi_0^2$ and the current density with $J_0 = \sigma_n \hbar / 2e\tau_0 \xi_0$.

For the sake of simplicity, we neglect intrinsic pinning effects and we assume $T=0$. Self-fields associated to the bias current and the screening effects are also neglected, otherwise an equation for the vector potential \mathbf{A} should be integrated in the above model. This simplification has been often used in the so-called high κ limit⁴⁶ and it is reasonable also for our sputtered Nb. In fact, in our Nb the coherence length is estimated $\xi \approx 13$ nm and the penetration depth $\lambda_L \approx 100$ nm at 4.2 K giving $\kappa \approx 8$. The condition $(i\nabla + \mathbf{A})\psi|_{\mathbf{n}} = 0$ is assumed for the order parameter at boundary, where \mathbf{n} is the unit vector normal to the contour of the superconductor. In order to inject a uniform bias current density J in our system we used conditions $-\nabla\varphi = (0, J)$ at the boundaries.

The effect of the ferromagnet on the superconductor enters through the vector potential \mathbf{A} in Eqs. (1) and (2). For the stray fields from stripe domains of fixed width ℓ aligned along x axis, a good approximation for the vector potential⁴² is

$$A_x(y) = 2h_s \ln \frac{\cosh \frac{\pi a}{\ell} + \cos \frac{\pi y}{\ell}}{\cosh \frac{\pi a}{\ell} - \cos \frac{\pi y}{\ell}}, \quad (3)$$

where a is the distance from the upper face of the ferromagnet. The origin of the x - y reference frame is assumed here and in the following in the center of the $L \times W$ superconducting film (see Fig. 5). To describe the modulation of stray fields at edges of the slab we assume the vector potential

$$A_y(x) = \frac{h_o}{h_r} \{ \text{atan}[h_r(x + W/2)] - \text{atan}[h_r(x - W/2)] - 2 \text{atan}(h_r W/2) \}. \quad (4)$$

According to Eqs. (3) and (4), the magnetic induction (describing stray fields) $\mathbf{B} = \nabla \times \mathbf{A}$ is vanishing but for the perpendicular component, given by

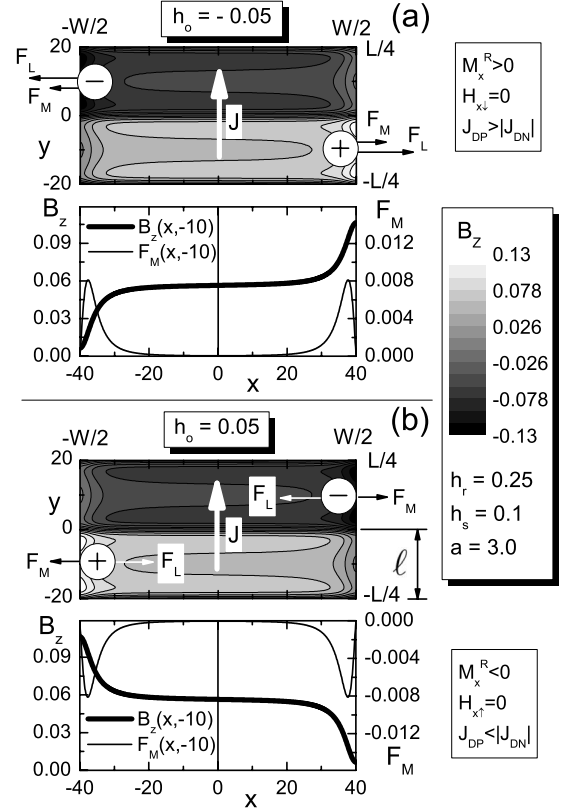


FIG. 5. (a) Gray scale plot of the stray magnetic fields $B_z(x, y)$ acting on the superconductor when the ferromagnet is in the remanent state at $H_{x1}=0$. A sketch of the forces acting on the vortices and antivortices nucleating in the superconductor is also shown. In the bottom panel there are shown the magnetic field profile $B_z(x, -10)$ and the magnetic force $F_M(x, -10)$ experienced by a vortex along the channel centered at $y=-10$. (b) Same as in (a) but the ferromagnet is now in the remanent state at $H_{x1}=0$.

$$B_z(x, y) = h_o [h_r^2(x + W/2)^2 + 1] - h_o [h_r^2(x - W/2)^2 + 1] - \frac{4\pi h_s \cosh \frac{\pi a}{\ell}}{\ell} \frac{\sin \frac{\pi y}{\ell}}{\sin^2 \frac{\pi y}{\ell} + \sinh^2 \frac{\pi a}{\ell}}. \quad (5)$$

To integrate the system, Eqs. (1) and (2), we make use of a finite-difference representation for the order parameter, vector potential, and electrostatic potential on a uniform Cartesian 129×129 space grid (corresponding to $W=L=80\xi_0$) and we employ a Dormand-Prince embedded method⁴⁷ for ordinary differential equations (an embedded Runge-Kutta integrator of order 8 with step size control) to find ψ . The electrostatic potential is obtained by the Fourier transform method.⁴⁷ When calculating the $E(J)$ [proportional to the $V(I)$] characteristics, we evaluated the electric field component E along current direction inside the superconducting sample at a distance $15\xi_0$ from the current injection interface. In this way the contact resistance at the interface is not taken into account and our results simulate a four-probe measurement. Initial conditions were $|\psi|=1$ and $\varphi=0$. The behavior of the system is studied on a large time scale so that time-averaged values are stationary.

In Fig. 5 we show a gray scale plot of the magnetic field $B_z(x, y)$ acting on the superconductor when the ferromagnet is in one of the two remanent states, as described by Eq. (5). For simplicity only one spatial period along y axis is represented. Bright (dark) regions are for field pointing in positive (negative) z direction. These stray field patterns mimic the ones of Fig. 4(a). Here a negative h_o parameter describes the state at $H_{x\downarrow}=0$ and a positive h_o the state at $H_{x\uparrow}=0$. In the micromagnetic simulations illustrated in Fig. 4, we found that the intensity of the stray fields is about 270 G at the center of the slab, rising to about ± 600 G at the edges. Noticing that in our Nb we estimate $H_{c1} \approx 300$ G at 4.2 K, the simulation parameters h_o and h_s are chosen so that the magnetic field is strong enough to nucleate vortices or antivortices at the edges of the film but not in the bulk of the film. In Fig. 5 we also show a sketch of the forces acting on the vortices and antivortices nucleating in the superconductor, as it helps to predict some results. Beside the Lorentz force associated to the transport current density, magnetic forces generated by the inhomogeneous magnetic field are present. Magnetic forces are proportional to the spatial gradient of the magnetic field $\mathbf{F}_M \propto \pm \nabla B_z(x, y)$, therefore in our patterns the vortices are attracted toward the brighter regions and the antivortices toward the darker regions. As an example, in the bottom panels of Figs. 5(a) and 5(b) there are shown the magnetic field profile $B_z(x, -10)$ and the associated magnetic force $F_M(x, -10) \propto \partial B_z(x, -10) / \partial x$ experienced by a vortex along the channel centered at $y=-10$ when the ferromagnet is in one of the two remanent states. Before to proceed further, we would comment on the possibility of presence of the ratchet effect in our system. The ratchet effect,^{20,24–28} that very often is at the origin of asymmetric response and rectifying effect, is characterized by a ratchet potential, i.e., a periodic potential that lacks spatial inversion symmetry. Beside the absence of a spatial periodicity along x , that should be a necessary condition for a “standard” ratchet, our potential $B_z(x, -10)$ exhibits an inversion symmetry along x . Precisely, but for an inessential additive constant, the $B_z(x, -10)$ is a simple odd function of x and it does not exhibit an asymmetric shape within the “spatial period”²⁴ $-W/2 < x < W/2$ that we could invoke to identify a ratchet. On the other hand, as can be seen Figs. 5(a) and 5(b), the magnetic force has ever same sign and same maximum intensity within a spatial period, differently from the forces originated from a standard ratchet potential,²⁴ characterized by alternating sign and variable strength so that their spatial average is zero over a spatial period.

With reference to the top panel of Fig. 5(a), vortices and antivortices are generated at edges and stay channeled in the respective bright and dark regions by the magnetic forces acting in the y direction. When a transport current density J is applied along the y direction, the Lorentz force pushes the vortices and the antivortices along the channels. When $J > 0$, magnetic force along the x direction and Lorentz force cooperate to prevent that vortices and antivortices enter the strip. In this case a large positive depinning current should be expected. When the current is reversed, $J < 0$, the magnetic force at the strip edges points again outward but the Lorentz force points toward the interior of the strip and, after the weak magnetic pinning force has been overcome, a station-

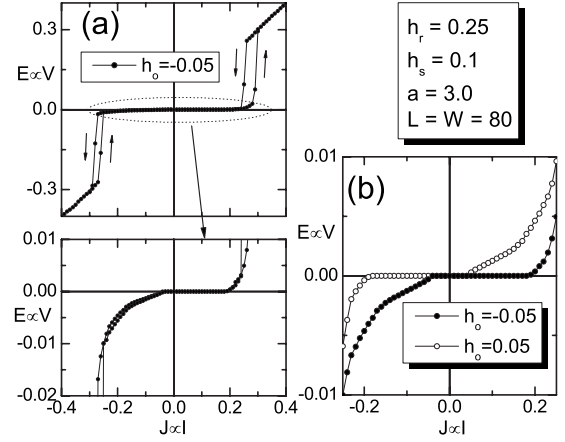


FIG. 6. (a) Calculated $E(J)$ curve of the superconductor while the ferromagnet is in the remanent state at $H_{x\downarrow}=0$. A blow up of the low-voltage region is also shown. (b) Comparison of the $E(J)$ curves corresponding to the two remanent states of the ferromagnet.

ary channeled flux motion regime can be established with associated onset of dissipation. This should account for the observed $I_{DP} > |I_{DN}|$ at $H_{\downarrow}=0$ in Fig. 1(b). The lower panel illustrates the situation in the other stable state, $M_x^R < 0$, achieved at $H_{x\uparrow}=0$. This time the Lorentz force associated to $J > 0$ moves the flux inward the strip and, after the weak magnetic force has been overcome, stationary flux motion is achieved with associated voltage generation. Instead, the Lorentz force associated to $J < 0$ adds to the magnetic force to prevent flux entry (and associated voltage generation), resulting in $I_{DP} < |I_{DN}|$ at $H_{\uparrow}=0$, coherently with the experimental results reported in Fig. 1(b).

Numerical results substantially confirm the above predictions. In Fig. 6(a) we plot the calculated $E(J)[V(J)]$ curve of the superconductor while the ferromagnet is in the state at $H_{x\downarrow}=0$ ($h_o < 0$). The positive and negative critical current densities differ only barely, in qualitative agreement with experimental results shown in Fig. 1(a). Notice that in our normalized units, the critical current density in the absence of perturbations (depairing current density) is $J_{depair}=0.36$ and the resistivity of normal state is $\rho_n=1$. The blow up of the low-voltage region, plotted in the lower panel of Fig. 6(a), confirms that a positive depinning current density substantially larger than the negative depinning current occurs. The calculated $E(J)$ curves corresponding to the two remanent states are compared in Fig. 6(b). The curve in one stable state is mirrored with respect to the origin in the other state, as in the experimental results shown in Fig. 1(b).

In the lower panel of Fig. 7 we show contour plots of the squared order parameter when we are in the marked points of the $E(J)$ curve at $H_{x\downarrow}=0$ shown above. Contour plots at left (right) correspond to negative (positive) current densities. The dark spots (local strong depression superconductivity) in these contour plots mark vortices or antivortices. In panel marked (3) $J=0.12$: vortices are nucleated at the right edge and antivortices at the left edge, but Lorentz force and magnetic pinning force point outward the strip and oppose flux entry, so that no electric field is generated. In panel (2) $J=-0.12$: now the Lorentz force points inward the strip and

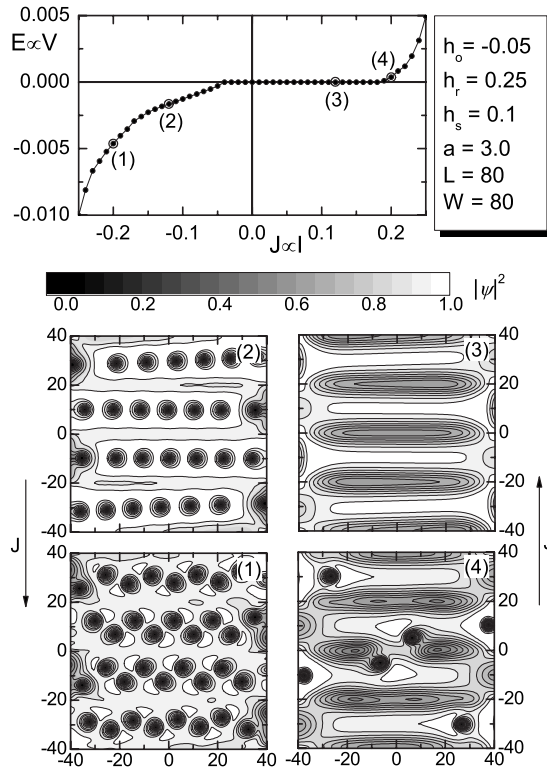


FIG. 7. Contour plots of the squared order parameter when we are on the marked points of the calculated $E(J)$ curve at $H_{x\perp}=0$ shown above.

has overcome the pinning magnetic force so that channeled flux motion is established and electric field is generated. Here vortex chains move from right to left and antivortex chains move from left to right. This is a nice example of a channeled flux flow regime with alternating vortex and antivortex chains moving in opposite directions in the strip. The flux flow regime⁴⁸ is characterized by an approximately linear $E(J)$ branch with slope proportional to flux density, as can be recognized in the calculated $E(J)$ curve and also in the experimental ones, to some extent. In panel (1) $J=-0.2$: we are again in a flux flow regime but now the flux density is doubled, as is doubled the slope of the corresponding branch in the $E(J)$ curve. The flux density increases despite the magnetic field is kept the same because when current density approaches the critical one the order parameter is depressed and the applied magnetic field is large enough to nucleate more vortices or antivortices than for lower current densities. In other words, the growth of the transport current density produces effects qualitatively similar to the increasing temperature. Finally, in panel (4) $J=0.2$: as in panel (1) the order parameter is quite depressed and the field in the bulk is now strong enough to nucleate vortex-antivortex pairs that Lorentz force pushes outward the strip, with associated generation of electric field.

Experimentally, we observed a decrease in the asymmetry in samples with a 50-nm-thick SiO_2 between Py and Nb, as shown in Fig. 2(b). This is consistent with the fact that the strength of stray fields from Py slab decreases with distance from the slab, as seen in also Fig. 4(c), and hence also the asymmetry they induce is decreased. We would notice that,

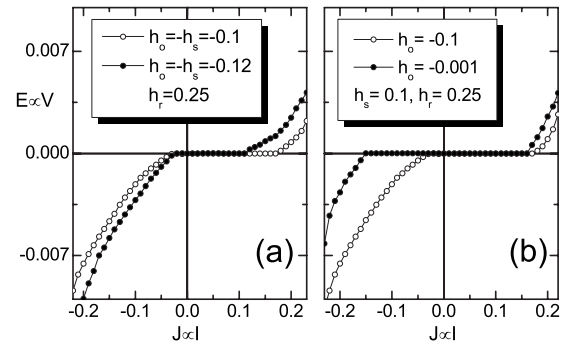


FIG. 8. (a) Calculated $E(J)$ curves with different magnetic field strength. In the curve with solid circles the magnetic field is strong enough to nucleate vortices and antivortices also in the bulk of the strip. (b) The $E(J)$ curve with stray fields at edges (open circles) is compared with the one with strongly reduced stray fields at edges (solid circles).

as can be envisaged from Fig. 4(c), the perpendicular component of the stray fields at center of the strip diminishes in approximately the thickness of the SiO_2 spacer layer by less than 50%, that is, it remains quite high. Nevertheless, the diodelike behavior is significantly decreased. This is due to the fact that also the strength of stray field at edges of the Py strip diminishes proportionally from about 600 G to approximately 300 G, that is, to a value that is only slightly larger than the critical field of Nb that at the working temperature of 4.72 K shown in Fig. 2(b) could be estimated to be around 250 G. So, the vortex generator effect of the stray fields at edges is significantly reduced and it is significantly reduced also the magnetic force at edges of the strip which is another cause of asymmetry.

The asymmetry of the depinning currents was found to vanish at a temperature $T_v < T_c$, as shown in Fig. 1(c) of our previous work.²⁹ This can be explained noticing that when T_c is approached the lower critical field of Nb decreases and stray fields, that in the experimental temperature range can be considered constant, can be strong enough to nucleate vortices and antivortices in the bulk of the Nb strip. This should result in a decrease in depinning currents and asymmetry because now the flux that can be affected by Lorentz force is already present in the Nb and the only cause of asymmetry comes from the weak magnetic pinning forces at ends of the channels. This effect is found also in the numerical simulations shown in Fig. 8(a). In the curve with open circles the magnetic field is, as in Fig. 7, such that vortices and antivortices are nucleated only at edges while, to simulate an increased temperature, for the curve with solid circles the magnetic field is strong enough to nucleate vortices and antivortices also in the bulk of the strip.

We also observed strong suppression of asymmetry when the width of Py layer was made several microns larger than the Nb layer, as seen in Fig. 2(c). In this case the stray fields at the edges of the Py slab, that decay inversely with distance from Py, are not strong enough to generate vortices at the edges of the Nb strip. Numerical simulations shown in Fig. 8(b) confirm this kind of asymmetry suppression.

As shown in Fig. 2(a), we do not observe asymmetry when the preparing field is applied parallel to the current

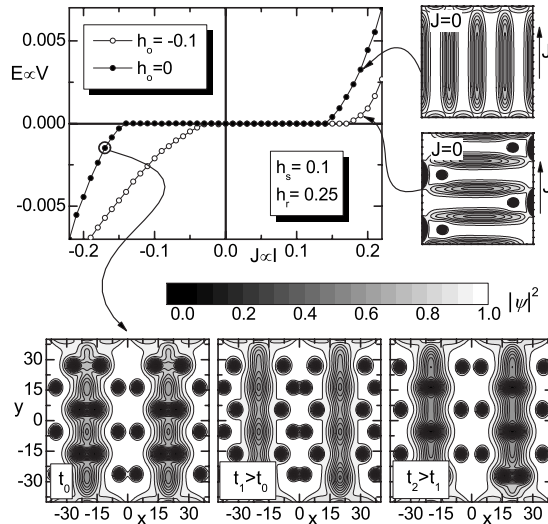


FIG. 9. $E(J)$ curves with current density perpendicular (open circles) or parallel (solid circles) to the channels. The contour plots of the squared order parameter shown the lower panel correspond to the marked point of the above $E(J)$ curve with current density applied parallel to the channels.

direction. This is consistent with the fact that in this case Lorentz force pushes vortices at edges where no stray field modulation is present, as suggested by contour plots in the right panels of Fig. 9. As in the experiments, the calculated $E(J)$ curve with current density parallel to the channels is found to be symmetric, as can be seen in the main panel of Fig. 9. We conclude noticing that for current parallel to the

channels the dissipative regime is different from the one we have found in the case of current perpendicular to channels. As can be recognized from the sequence of contour plots shown in the bottom panels of Fig. 9, now the dissipation is due to nucleation of bound vortex-antivortex pairs in the channels ($t=t_0$). Lorentz force breaks the pairs and then moves the free vortices and antivortices from next-neighbor pairs one toward the other causing them to annihilate in a collision ($t=t_1$). The whole process restarts with nucleation of new bound vortex-antivortex pairs ($t=t_2$).

IV. SUMMARY

Summarizing, we have further investigated the bistable vortex diode made of a ferromagnet-superconductor bilayer that we have recently demonstrated. With the help of numerical simulations, we analyzed in detail the main physical mechanism involved in the bistable diode. Micromagnetic simulations, performed using the Landau-Lifshitz-Gilbert model for the ferromagnet, and vortex dynamics of the superconductor, simulated using the two-dimensional time-dependent Ginzburg-Landau equation, confirm that the observed bistable diode behavior can be accounted for by the stray fields from the ferromagnetic layer that generate an asymmetric and bistable magnetic forces background for the Abrikosov vortices moving in the superconducting layer. In the dissipative branch of the bilayer, a peculiar channeled flux flow regime is achieved, with alternating vortex and antivortex chains moving in the opposite directions in the superconducting layer.

*Corresponding author; giocar@sa.infn.it

- ¹A. I. Buzdin, *Rev. Mod. Phys.* **77**, 935 (2005).
- ²I. F. Lyuksyutov and V. L. Pokrovsky, *Adv. Phys.* **54**, 67 (2005).
- ³A. Yu Aladyshkin, A. V. Silhanek, W. Gillijns, and V. V. Moshchalkov, *Supercond. Sci. Technol.* **22**, 053001 (2009).
- ⁴J. Y. Gu, C. Y. You, J. S. Jiang, J. Pearson, Ya. B. Bazaliy, and S. D. Bader, *Phys. Rev. Lett.* **89**, 267001 (2002).
- ⁵I. C. Moraru, W. P. Pratt, Jr., and N. O. Birge, *Phys. Rev. Lett.* **96**, 037004 (2006).
- ⁶A. Singh, C. Sürgers, and H. v. Lohneysen, *Phys. Rev. B* **75**, 024513 (2007).
- ⁷V. Peña, Z. Sefrioui, D. Arias, C. Leon, J. Santamaria, J. L. Martinez, S. G. E. te Velthuis, and A. Hoffmann, *Phys. Rev. Lett.* **94**, 057002 (2005).
- ⁸N. M. Nemes, M. Garcia-Hernandez, S. G. E. te Velthuis, A. Hoffmann, C. Visani, J. Garcia-Barriocanal, V. Peña, D. Arias, Z. Sefrioui, C. Leon, and J. Santamaria, *Phys. Rev. B* **78**, 094515 (2008).
- ⁹T. Hu, H. Xiao, C. Visani, Z. Sefrioui, J. Santamaria, and C. C. Almasan, *Physica B* **403**, 1167 (2008).
- ¹⁰T. W. Clinton and M. Johnson, *Appl. Phys. Lett.* **70**, 1170 (1997).
- ¹¹C. Bell, S. Tursucu, and J. Aarts, *Phys. Rev. B* **74**, 214520 (2006).
- ¹²R. Steiner and P. Ziemann, *Phys. Rev. B* **74**, 094504 (2006).
- ¹³D. Stamopoulos, E. Manios, and M. Pissas, *Phys. Rev. B* **75**, 184504 (2007).
- ¹⁴G. Carapella, F. Russo, and G. Costabile, *Phys. Rev. B* **78**, 104529 (2008).
- ¹⁵F. Russo, G. Carapella, and G. Costabile, *Supercond. Sci. Technol.* **22**, 055015 (2009).
- ¹⁶M. van Zalk, M. Veldhorst, A. Brinkman, J. Aarts, and H. Hilgenkamp, *Phys. Rev. B* **79**, 134509 (2009).
- ¹⁷D. Y. Vodolazov, B. A. Gribkov, S. A. Gusev, A. Yu. Klimov, Yu. N. Nozdrin, V. V. Rogov, and S. N. Vdovichev, *Phys. Rev. B* **72**, 064509 (2005).
- ¹⁸R. M. Ainbinder and I. L. Maksimov, *Supercond. Sci. Technol.* **20**, 441 (2007).
- ¹⁹N. Touitou, P. Bernstein, J. F. Hamet, Ch. Simon, L. Méchin, J. P. Contour, and E. Jacquet, *Appl. Phys. Lett.* **85**, 1742 (2004).
- ²⁰G. Carneiro, *Physica C* **432**, 206 (2005).
- ²¹P. S. Swartz and H. R. Hart, *Phys. Rev.* **137**, A818 (1965).
- ²²P. S. Swartz and H. R. Hart, *Phys. Rev.* **156**, 412 (1967).
- ²³F. Raissi and J. E. Nordman, *Appl. Phys. Lett.* **65**, 1838 (1994).
- ²⁴C.-S. Lee, B. Jankó, I. Derényi, and A.-L. Barabási, *Nature (London)* **400**, 337 (1999).
- ²⁵G. Carapella and G. Costabile, *Phys. Rev. Lett.* **87**, 077002 (2001).

- ²⁶J. E. Villegas, S. Savel'ev, F. Nori, E. M. Gonzalez, J. V. Anguita, R. Garcia, and J. L. Vicent, *Science* **302**, 1188 (2003).
- ²⁷J. Van de Vondel, C. C. de Souza Silva, B. Y. Zhu, M. Morelle, and V. V. Moshchalkov, *Phys. Rev. Lett.* **94**, 057003 (2005).
- ²⁸C. C. de Souza Silva, A. V. Silhanek, J. Van de Vondel, W. Gillijns, V. Metlushko, B. Ilic, and V. V. Moshchalkov, *Phys. Rev. Lett.* **98**, 117005 (2007).
- ²⁹G. Carapella, V. Granata, F. Russo, and G. Costabile, *Appl. Phys. Lett.* **94**, 242504 (2009).
- ³⁰Z. Yang, M. Lange, A. Volodin, R. Szymczak, and V. V. Moshchalkov, *Nature Mater.* **3**, 793 (2004).
- ³¹W. Gillijns, A. Yu. Aladyshkin, M. Lange, M. J. Van Bael, and V. V. Moshchalkov, *Phys. Rev. Lett.* **95**, 227003 (2005).
- ³²L. Y. Zhu, T. Y. Chen, and C. L. Chien, *Phys. Rev. Lett.* **101**, 017004 (2008).
- ³³J. Ben Youssef, N. Vukadinovic, D. Billet, and M. Labrune, *Phys. Rev. B* **69**, 174402 (2004).
- ³⁴A. Belkin, V. Novosad, M. Iavarone, J. Fedor, J. E. Pearson, A. Petrean-Troncalli, and G. Karapetrov, *Appl. Phys. Lett.* **93**, 072510 (2008).
- ³⁵V. K. Vlasko-Vlasov, U. Welp, A. Imre, D. Rosenmann, J. Pearson, and W. K. Kwok, *Phys. Rev. B* **78**, 214511 (2008).
- ³⁶V. V. Vlasko-Vlasov, U. Welp, G. Karapetrov, V. Novosad, D. Rosenmann, M. Iavarone, A. Belkin, and W.-K. Kwok, *Phys. Rev. B* **77**, 134518 (2008).
- ³⁷A. V. Silhanek, J. Van de Vondel, A. Leo, G. W. Ataklti, W. Gillijns, and V. V. Moshchalkov, *Supercond. Sci. Technol.* **22**, 034002 (2009).
- ³⁸J. Van de Vondel, A. V. Silhanek, V. Metlushko, P. Vavassori, B. Ilic, and V. V. Moshchalkov, *Phys. Rev. B* **79**, 054527 (2009).
- ³⁹A. Nemoto, Y. Otani, S. G. Kim, K. Fukamichi, O. Kitakami, and Y. Shimada, *Appl. Phys. Lett.* **74**, 4026 (1999).
- ⁴⁰B. B. Pant and K. N. Matsuyama, *Jpn. J. Appl. Phys.* **32**, 3817 (1993).
- ⁴¹OOMMF, Object Oriented Micromagnetic Framework, <http://math.nist.gov/oommf>
- ⁴²G. M. Maksimova, R. M. Ainbinder, and D. Yu. Vodolazov, *Phys. Rev. B* **78**, 224505 (2008).
- ⁴³D. Y. Vodolazov, F. M. Peeters, S. V. Dubonos, and A. K. Geim, *Phys. Rev. B* **67**, 054506 (2003).
- ⁴⁴D. Y. Vodolazov, F. M. Peeters, I. V. Grigorieva, and A. K. Geim, *Phys. Rev. B* **72**, 024537 (2005).
- ⁴⁵L. Kramer and R. J. Watts-Tobin, *Phys. Rev. Lett.* **40**, 1041 (1978).
- ⁴⁶Q. Du and P. Gray, *SIAM J. Appl. Math.* **56**, 1060 (1996).
- ⁴⁷W. H. Press, S. A. Teukolsky, W. T. Vetterling, and B. P. Flannery, *Numerical Recipes: The Art of Scientific Computing*, 3rd ed. (Cambridge University Press, Cambridge, England, 2007).
- ⁴⁸G. Blatter, M. V. Feigelman, V. B. Geshkenbein, A. I. Larkin, and V. M. Vinokur, *Rev. Mod. Phys.* **66**, 1125 (1994).